Energy Engineering

Tech Science Press

https://doi.org/10.32604/ee.2026.086266

ARTICLE

Identification of the Flow Structure in Normal and Aggressive S-Shaped Diffusers of the Aeroengine Intake by Flow Visualization Methods

Hussain H. Al-Kayiem[1,*], Ali M. Mohsen[2], Ajyal A. Hassan Jallout[3], Ali M. Tukkee[4,5] and Raed A. Jessam[6]

[1]College of Engineering Technologies, University of Hilla, Hillah, Babylon, Iraq
[2]School of Engineering, Faculty of Innovation and Technology, Taylor's University, Subang Jaya, Malaysia
[3]College of Mechanical Engineering, University of Technology—Iraq, Baghdad, Iraq
[4]Department of Petroleum Engineering, University of Kerbala, Karbala, Iraq
[5]College of Advanced Technologies, University of Warith Al-Anbiyaa, Karbala, Iraq
[6]College of Electromechanical Engineering, University of Technology—Iraq, Baghdad, Iraq

*Corresponding Author: Hussain H. Al-Kayiem. Email: hussain.alkayiem@hilla-unc.edu.iq or prof.hussain@acaress.org

Received: 27 May 2026; Accepted: 02 July 2026; Published: 12 November 2026

ABSTRACT: The gas turbine intake, including the S-shaped diffuser must be as short as possible to reduce the aeroengine size and weight. Reducing the length of the bare S-shaped diffuser (BD) results in an aggressive diffuser (AD) with risk of large flow separation and reduced performance. This study aims to investigate and characterize the flow structure, particularly the flow reversal and its separation, in S-shaped diffusers. Flow visualization was achieved using experimental flow visualization with wall-mounted tufts and CFD simulation of the flow field for five models, including BD, AD and AD/VG, fitted with three different types of vortex generators (VGs). The selected VGs are type 1: co-rotating low-profile, type 2: co-rotating streamline sheet, and type 3: trapezoidal. All have been installed at a high-curvature location within the diffusers, designated as plane 5. All experimental tests and computational simulations were performed with an inlet Reynolds number of 40,000. The experimental diffuser models were simulated using ANSYS FLUENT 15, employing the 3D standard k-ε turbulence model to capture flow structures that cannot be visualized by experimental methods. Results revealed the capability of the adopted methods to identify the separation points and the flow structure of each tested case. The separation points were approximately located at dimensionless positions, $X_{s.p./}$diffuser length, of 0.4, 0.3, 0.678, and 0.78, experimentally, and 0.406, 0.314, 0.638, and 0.8, numerically, for BD, AD, and AD/VG-1, and AD/VG-3, respectively. The results show increased distortion of the AD compared to the BD by 11.9%, experimentally and 9.6% numerically. Experimentally, the destruction is reduced by 71.8%, 87.8%, and 29.7% by VG-1, VG-2, and VG-3, respectively, and computationally by 44.6%, 88%, and 36.2% by VG-1, VG-2, and VG-3, respectively. The results show that VGs type-2 provides the largest improvement in flow structure by suppressing flow separation to the maximum extent and increasing flow uniformity at the diffuser outlet.

KEYWORDS: Energy conversion system; flow visualization; gas turbine; S-shaped diffuser; vortex generator

1 Introduction

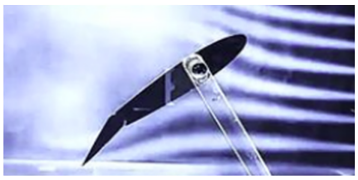
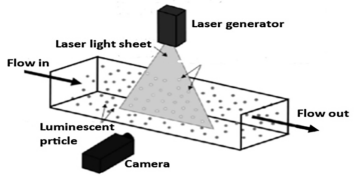
The study of the S-shaped diffuser is a prevailing research subject in mechanical engineering because of the important applications in aeroengines [1]. The general configuration of any S-shaped diffuser has a centerline curvature and an increase in cross-sectional area along its length, leading to cross-stream pressure gradients that can produce significant secondary flows resulting in a non-uniform pressure profile at the

Copyright © 2027 The Authors. Published by Tech Science Press. This work is licensed under a Creative Commons Attribution 4.0 International License, which permits unrestricted use, distribution, and reproduction in any medium, provided the original work is properly cited.

Aerodynamic Inlet Plane (AIP) of the aeroengine. Furthermore, the adverse streamwise pressure gradient, caused by an increasing cross-sectional area, may also lead to reversal flow and flow separation [2]. A properly designed diffuser should efficiently decelerate the incoming flow. To achieve a convenient performance, S-shaped diffusers must also sustain minimal total pressure losses and deliver nearly uniform flow with small crossflow velocity components at the AIP. Therefore, an aircraft designer often faces a complex dilemma between reducing length and its consequences for pressure recovery. Size and weight constraints encourage the use of a short S-shaped diffuser, named "S-shaped aggressive diffuser". However, this reduction would result in greater streamline curvature, larger adverse pressure gradients and the risk of unacceptable duct performance [3].

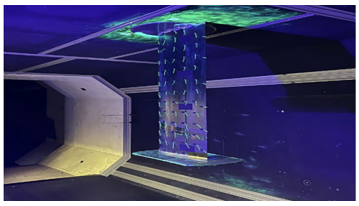
Flow visualization techniques are essential for identifying complex flow structures, such as separation, reversal flow, and vortex formation, in normal and aggressive S-shaped aeroengine diffusers. These methods, both experimental and computational, show that aggressive S-ducts, characterized by high deflection and short length, generate intense adverse pressure gradients, causing stronger, more persistent counter-rotating vortices (often identified as a pair) and significant flow non-uniformity at the engine face [4–6]. Flow visualization techniques might be experimental or computational. In experimental techniques, flow visualization could be achieved by one of the methods described in Table 1.

Table 1: Samples of flow visualization techniques.

Technique	Description	Sample of Usage	
Smoke Visualization	A heavy smoke, often produced by dry ice or a smoke generator, is injected into the air stream in wind tunnels to visualize the flow patterns and the separation zones.		Flow field over a wing with flap [7]
Particle Image Velocimetry (PIV)	PIV uses tracer particles (like polyvinylchloride) and a laser split beam in liquid-bound flow. With a high-speed camera, it is possible to capture the flow field structure.		layout of the PIV technology
Surface Oil/Paint	It could be achieved by coating the surface with a mix of tracers, formed from kerosene and paint, to visualize boundary layer separation and flow reversal.		Qualitative observation of oil mist passing though the wave plates [8]

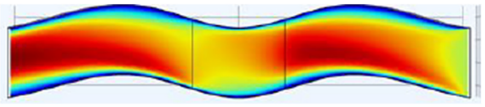
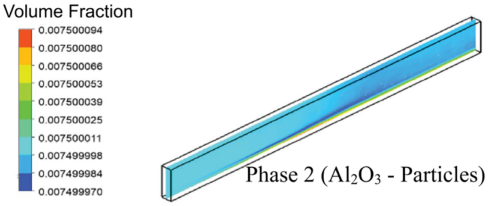
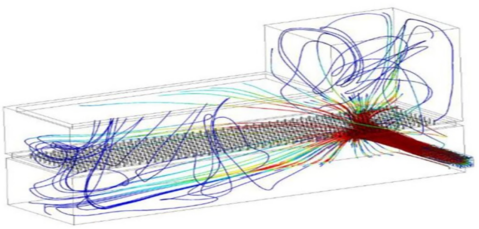
(Continued)

Table 1 (continued)

Technique	Description	Sample of Usage	
Tufts	Used to observe flow separation and the reversal of flow direction over surfaces, like airfoils, airplane models, buildings models, diffusers, nozzles, . . ., etc.		Flow field over unsteady loaded airfoil [9]

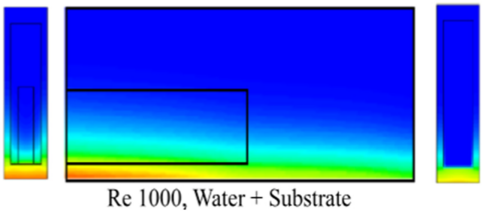
Using the computational fluid dynamics (CFD) technique, flow visualization could be achieved by one of the methods listed in Table 2. Creation of velocity contours and streamlines: Used to map out the flow field, showing the formation of high-velocity streaks, stagnant regions, and vortex cores, often utilizing the Reynolds Stress Model (RSM) or RNG models to accurately predict complex flow in aggressive geometries. Total pressure recovery contours could be used to visualize the distortion of flow at the Aerodynamic Interface Plane (AIP) of aeroengines [10,11].

Table 2: Flow visualization techniques by computational fluid dynamic simulation.

Technique	Description	Sample of Usage
Velocity Contours and Velocity Vectors	Graphical representations show how flow speed changes across a space by graded colors. It could identify regions of high and low speed in the flow field. Separation zones could also be identified.	 Velocity contours in a wavey duct [12]
Volume Fraction	Flow visualization by volume fraction is used to investigate the distribution of nanoparticles in microchannels.	 Volume fraction in microchannels with nanofluid flow [13]
Streamlines	Streamlines are lines that are tangent to the velocity vector of the flow. They show the instantaneous direction of a fluid flow at a specific moment in time.	 The CFD simulation results of streamline of air velocity in dryer [14]

(Continued)

Table 2 (continued)

Technique	Description	Sample of Usage
Thermal and Pressure Distribution Contours	Thermal and pressure contours in an engineering device allow the realization of the hydrodynamic process understanding. They permit the identification of stagnation points, pressure difference, occurrence of shock waves, and circulation.	 Thermal distribution in microchannel heat exchanger [13]

However, tufts could be utilized for flow over objects to approximate the instantaneous local flow direction near the surface, as they are cheap and easy to implement. Tufts can be of many types that may have specific drag, inertia, and stiffness, which affect the response to the flow behavior. The specific tufting method of tufts on a surface can also influence a tuft's ability to indicate the local flow direction [15]. These and other shortcomings have largely precluded the use of tufts to obtain quantitative data. Surface flow visualization is typically used to compare and validate computational simulations by experiments flow visualization [16,17]. Nonetheless, some investigations have shown that tufts could be used to obtain quantitative flow field results.

Tufts were used for the identification of separated flow behind a backward-facing step [18] and for the characterization of the flow on full-scale wind turbines, for which the small fraction is of interest [19,20]. The studies by [19,20] demonstrated the ability of tufts, combined with a camera and image processing, to yield quantitative results. More detailed quantitative information has been obtained from tufts by using them to measure velocity fields or identify pressure fluctuations based on the deflection of tufts [21]. However, they have identified issues associated with tufts in flow fields with low velocity or high oscillations.

This paper presents visualization of the flow in S-shaped diffusers as a critical engineering structure in the aeroengine. The flow visualization and identification of the separation point and the reversal flow have been achieved through a combination of experimental measurement and computational simulation of the S-shaped diffuser. The flow field was investigated with an inlet airflow at a Reynolds number (Re) of 40,000. Five different S-shaped diffuser cases were studied using flow visualization, including a bare case and an aggressive case. They enhanced aggressive S-shaped diffusers with vortex generators (VGs), also known as energy promotors (EPs). The enhanced aggressive diffuser was examined using three different types of VGs.

This work contributes to the field of fluid dynamics generally and aeroengine design, particularly. There are experimental and numerical investigations and predictions of the S-shaped diffuser, but analysis of such configurations using flow visualization is not available in the literature. The work contributes to improving aeroengine design by reducing intake size and mitigating separation-induced losses through the installation of vortex generators. Many types of vortex generators have been included in the investigation, and an important conclusion has been drawn on the best type to be used.

2 Research Methodology

The methodologies adopted in this investigation to visualize the flow inside the S-shaped diffusers are experimental and computational visualization techniques. The experimental visualization method used experimental models, while the computational method used a developed simulation procedure utilizing ANSYS FLUENT 15 commercial software.

2.1 Nondimensionalization of Performance Parameters

Two nondimensional parameters have been used in the mesh dependency check, the validation of the computational procedure, and in the discussion and comparison of results.

2.1.1 Wall Static Pressure Recovery Coefficient

The wall static pressure recovery coefficient (C_{WPR}) is widely used in the investigations of the S-shaped diffusers to compare various design and operational conditions. It represents the static pressure difference at a certain point in the wall and the static pressure at the diffuser inlet divided by the mean dynamic head at the inlet, as in Eq. (1) [3,4]

$$C_{WPR} = \frac{p_{ws} - p_{wsi}}{\frac{1}{2}\rho U_{av.i}^2} \tag{1}$$

2.1.2 Distortion Coefficient

The distortion coefficient, $DC(45°)$, is an important parameter for evaluating the performance of an S-shaped diffuser. It represents the difference between the maximum and minimum total pressures divided by the average total pressure at the diffuser outlet plane. All the pressures in Eq. (2) are the ones at the outlet of the diffuser.

$$DC(45°) = \frac{p_{t.max} - p_{t.min}}{p_{t.ave}} \tag{2}$$

2.1.3 Dimensionless Geometries

Allocation of the planes, shown in Fig. 1, and the location of the separation point are identified using the dimensionless geometry method by dividing the location on the axial axis, $X_{s.p.}$, by the diffuser test section length, L_s. The L_s are 396 and 280 mm for the BD and AD, respectively. Hence, the location of the separation point, $L_{s.p.}$ and planes, L_{pi}, could be generalized as defined in Eqs. (3a) and (3b).

$$L_{s.p.} = \frac{X_{sp}(mm)}{396(mm)}; \qquad L_{pi} = \frac{X_{p.i}(mm)}{396(mm)} \qquad \text{for the bare S – shaped diffuser} \tag{3a}$$

$$L_{s.p.} = \frac{X_{sp}(mm)}{280(mm)}; \qquad L_{pi} = \frac{X_{p.i}(mm)}{280(mm)} \qquad \text{for aggressive S – shaped diffuser} \tag{3b}$$

All dimensions are along the horizontal x-axis, where $i = 1, 2, \ldots, 9$. This nondimensionalization means that $L_{p1} = 0$ and $L_{p9} = 1$.

2.2 Investigation Cases

The flow structure within S-shaped diffusers has been visualized in different configurations. The geometrical parameters that describe bare and aggressive diffusers are shown in Fig. 1.

The geometry specifications of the BD and AD models are summarized in Table 3, following the symbols in Fig. 1.

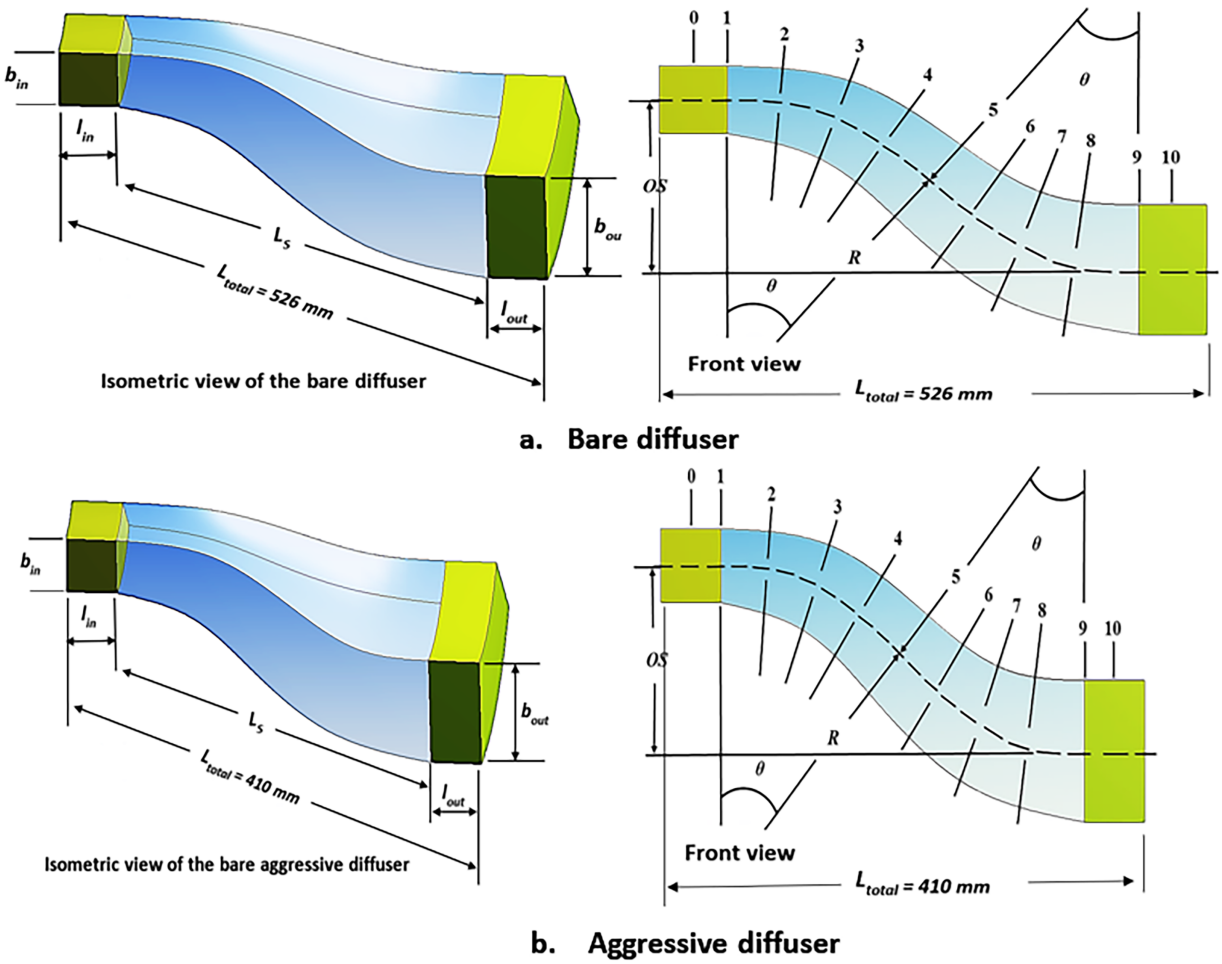


Figure 1: Configurations of the: (**a**) bare S-shaped diffuser, (**b**) aggressive S-shaped diffuser.

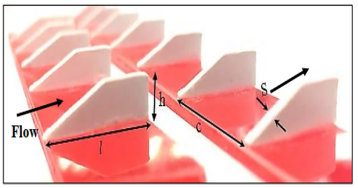
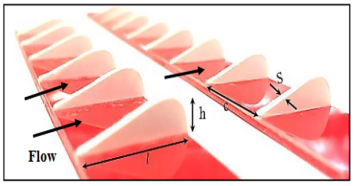
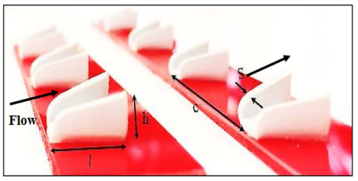
Table 3: Geometries of the bare D and the AD diffuser models.

Parameter	Bare D	Bare AD & AD/EP
Inlet area conduit height, b_i	65 mm	65 mm
Inlet area conduit length, l_i	65 mm	65 mm
Outlet area conduit height, b_o	125 mm	125 mm
Outlet area conduit length, l_o	65 mm	65 mm
Area ratio, AR (A_o/A_i)	3.1	3.1
Model total length, L_{total}	526 mm	410 mm
Test section length, L_S	396 mm	280 mm
Test section turning angle, θ	45°/45°	35.3°/35.3°
Centerline turning radius, R	280 mm	242.5 mm
Planes of measurements	[0, 1, 2, 3, 4, 5, 6, 7, 8, 9, and 10]	

Due to the large energy losses often associated with boundary-layer separation, passive flow control remains very important for many technological applications [22,23]. The VGs are fixtures with heights

ranging from 10% to 50% of the boundary layer thickness, δ. The boundary layer thickness has been measured experimentally and found to be about 13 mm at the inflection plane 5 using hot wire anemometry. Three types of VGs were used to investigate the effectiveness of their geometries on the performance enhancement of bare AD. The VGs were made from 1.0 mm thick high-impact polystyrene sheets using a CNC machine. The shapes and geometries of the investigated VGs are described in Table 4.

Table 4: Types of vortex generators installed at plane 5 inside the bare aggressive diffuser.

Type of VG	Description	H (mm)	*L* (mm)	S (mm)	C (mm)	
Type-1 VG-1	Co-rotating low-profile VG	5	20	1	22	
Type-2 VG-2	Co-rotating streamline sheet VG	5	20	1	20	
Type-3 VG-3	Trapezoidal submerged VG	5	12	1	32	

2.3 Experimental Implementation

The experiments were performed in the Advanced Fluid Dynamic Lab at Universiti Teknologi PETRONAS (UTP), Malaysia. The test section corresponds to one of the eight sections of the annulus S-shaped diffuser. Two models have been designed and fabricated.

2.3.1 Experimental Setup

The test models in the current investigation are unique as they have been fabricated from a real section of the S-shaped diffuser, unlike earlier works which used a rectangular cross-section. The upper and lower parts of the test sections were made of solid wood cut to shape by a CNC machine, as shown in Fig. 2a. The sides were made of Perspex sheets to allow observation and image capturing, as shown in Fig. 2b.

In the current investigation, the VGs were fitted at plane 5, as the experimental measurements of [6] and the numerical simulation of [24] showed that the aggressive diffuser performs optimally when the VGs were installed at plane 5. The number of VGs installed on plane 5 was 5 for type-1, 6 for type-2, and 4 for type-3. The difference in the number of installed VGs is due to the VGs' sizes.

In summary, the five visualized cases, experimentally and numerically, of the bare S-shaped diffuser (BD), aggressive S-shaped diffuser (AD), aggressive S-shaped diffuser with VG type-1 (AD/VG-1), aggressive S-shaped diffuser with VG type-2 (AD/VG-2), and aggressive S-shaped diffuser with VG type-3 (AD/VG-3)

are described in Table 5. Note that all VGs cases are fitted in plane 5, and all have been tested with air flowing at Re = 40,000.

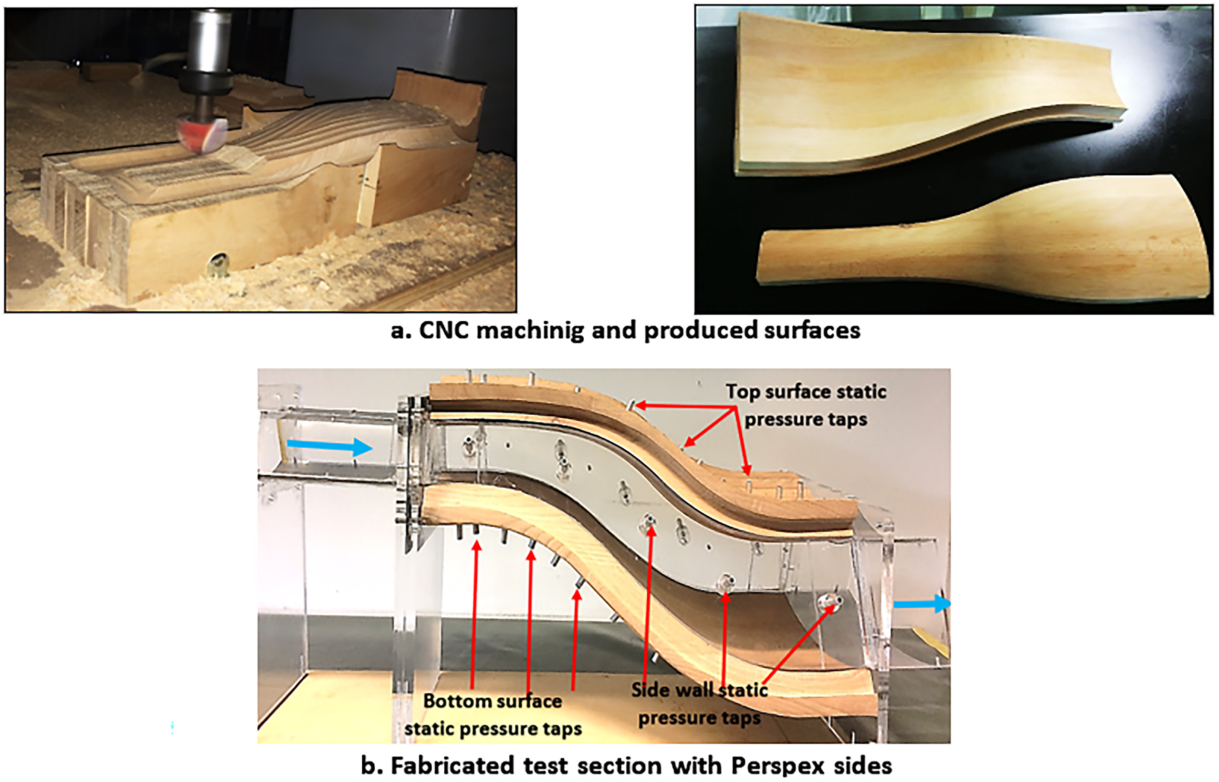


Figure 2: The fabrication details of the test section of the S-shaped diffuser. (**a**) CNC machining and produced surfaces, and (**b**) the final assembled and fabricated test section.

Table 5: Summary of investigated cases by flow visualization.

Code	Case of S-Shaped Diffuser	Info	Main Geometrical Characteristic	Reference Figure
BD	Bare diffuser	Experimental and Numerical Re = 40,000	Total length: 526 mm Curved sections: 396	Fig. 1a
AD	Aggressive diffuser		Total length: 410 mm Curved sections: 280	Fig. 1b
AD/VG-1	Aggressive diffuser fitted with VG type-1		Total length: 410 mm Curved sections: 280	Fig. 1b with VG type-1 in Table 4
AD/VG-2	Aggressive diffuser fitted with VG type-2		Total length: 410 mm Curved sections: 280	Fig. 1b with VG type-2 in Table 4
AD/VG-3	Aggressive diffuser fitted with VG type-3		Total length: 410 mm Curved sections: 280	Fig. 1b with VG type-3 in Table 4

The experimental setup is shown in Fig. 3. It includes four main components: air supply unit, flow stabilization section, S-shaped diffuser test section, and the measurement instrumentation system. The air supply unit consists of air blowers, flexible joint and a ball valve to control variable airflow. The flow stabilization section included air duct, honeycomb and screen to ensure uniform inlet airflow conditions.

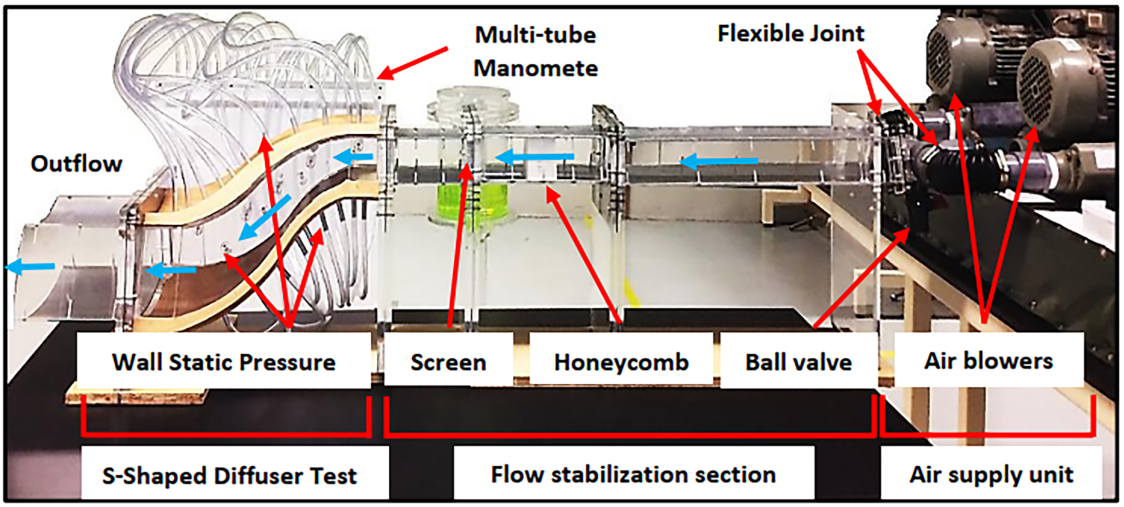


Figure 3: Image of the experimental setup.

2.3.2 Flow Visualization by Wall-Mounted Tufts

Experimental flow visualization was achieved using wall-mounted tufts. The wall-mounted tufts are a simple means of estimating the direction of flow near the solid surface by attaching one end of short tufts to the body surface. Black color tufts were distributed in separate lines at different planes (see plane locations in Fig. 1), and mounted on the surface using a very thin 0.5 mm sticker to avoid boundary-layer disturbances. A simple camera captured the tufts' fluctuations, and the images were used to analyze the flow structure and approximate separation points, if present.

2.3.3 Measuring Instrumentation and Uncertainties

To predict the wall static pressure coefficient and destruction coefficient, as well as the inlet Re and turbulence intensity, the velocity and pressure should be measured. A datalogger KIMO-Multifunction AMI300, a portable hotwire probe, a static pressure probe, and a multi-tube manometer have been used. The multi-tube manometers were calibrated using an inclined manometer (AIRFLOW Type 5 manometer). The mean deviations between the inclined manometer and the multi-tube manometer are ±5.3% and ±4.8% at different points on the top and bottom surfaces, respectively. The inflow dynamic pressure, inlet velocity, and turbulence intensity were measured using a pitot-static probe and a hotwire anemometer, both connected to a KIMO Multifunction AMI300.

The datalogger has an accuracy of ±0.5% of the reading. The pressure probe's accuracy is ±0.2% per supplier. Hence, the pressure measurement accuracy is around ±0.57%. The accuracy of the hotwire probe used for velocity measurements is ±0.03%, as provided by the supply company. Hence, the possible error in the velocity is around ±0.55%.

2.4 Flow Visualization by Computational Simulation

Computational visualization has been used as a complement to experimental visualization, providing insight into the flow structure near the surface. Steady, 3D incompressible flow models of BD, AD and AD/EP have been generated using the ANSYS 15 DesignModeler. The models simulate the actual experimental conditions. All have been run under inlet Re = 40,000. Further details of the computational procedure are reported in [24]. The CFD simulation and analysis adopted the standard k-ε based on comparison analysis and recommendations made by [24,25].

2.4.1 Computational Model Meshing and Mesh Independency Check

Mesh generation or discretization means subdividing the physical domain of the flow field into separate subdomains, computational cells, or control volumes. The mesh was an unstructured type containing elements of different shapes and sizes, as shown in Fig. 4.

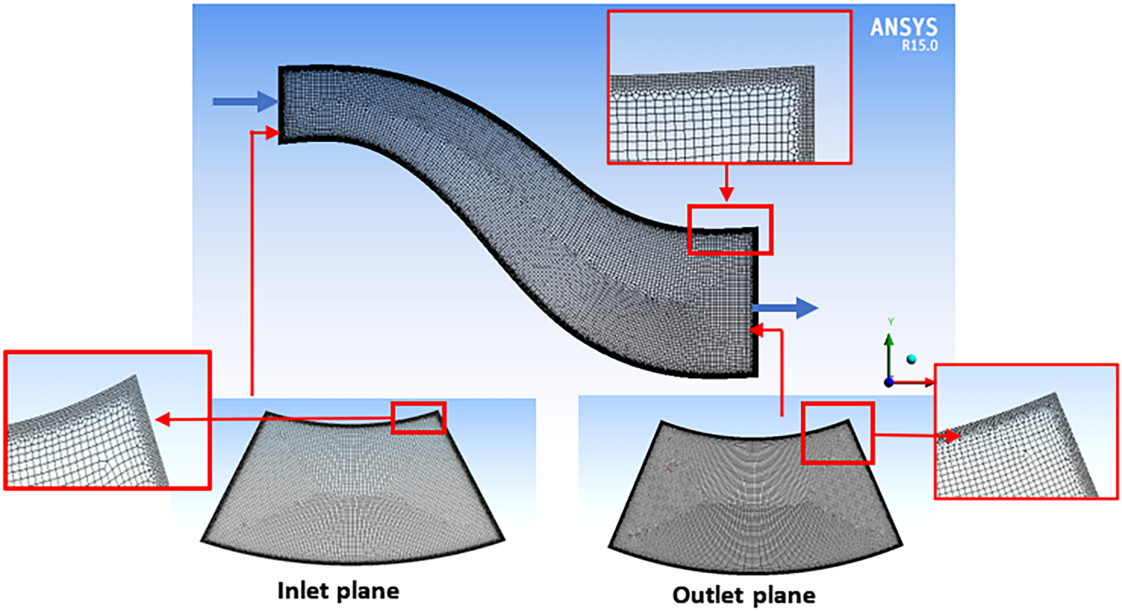


Figure 4: Unstructured mesh of AD.

To determine the optimal mesh or an accurate solution, a study of mesh refinement was conducted to select the optimal number of elements for the model. A mesh independence study based on the wall static pressure coefficient, C_{WPR}, to select the optimum number of elements, i.e., the mesh size. To perform a mesh independence study, the model was initially developed with 183,402 elements (a coarse mesh), by default. Changes in the mesh size and the comparison results are presented in Table 6.

When the default mesh increased to 214,417 elements (medium mesh), the difference in C_{WPR} prediction is around 4.3%. Further increase in the number of elements to fine mesh with 666,976 elements shows 4.5% compared to the medium mesh. More increase in the elements to finer mesh, with 708,603 elements, and finest mesh, with 843,827 elements, show a change in the differences by 2.35% and 1.2%, respectively. Compared with the experimental measurement results of the C_{WPR}, the absolute percentage of differences are 18%, 14%, 10%, 8%, and 7% for the default, medium, fine, finer, and finest meshes, respectively. Therefore, 708,603 elements are used as the optimum number of mesh for the simulation of all other cases, as

the difference between the finer mesh and finest mesh in C_{WPR} values is 1.2% and the comparison with experimental results is 8% absolute percentage of error.

Table 6: Top wall static pressure recovery coefficient, C_{WPR} variation with refining the grid of AD/EP with VGs type-2 at plane 5, compared to the experimental case.

Number of Elements		Type of Mesh				
		Coarse 183,402	**Medium 214,417**	**Fine 666,976**	**Finer 708,603**	**Finest 843,827**
C_{WPR} on top surface	Exp.			0.77		
	CFD	0.93	0.89	0.85	0.83	0.82
Appr. error %		–	4.3%	4.5%	2.35%	1.2%

The effect of different mesh configurations on the variation of C_{WPR} on the top and bottom surfaces is calculated for each mesh configuration, as shown in Fig. 5. The information from the figures shows that the C_{WPR} containing 708,603 elements is in reasonable agreement with the experiment. Table 6 shows the comparison between the numerical and experimental results of C_{WPR} with different types of mesh.

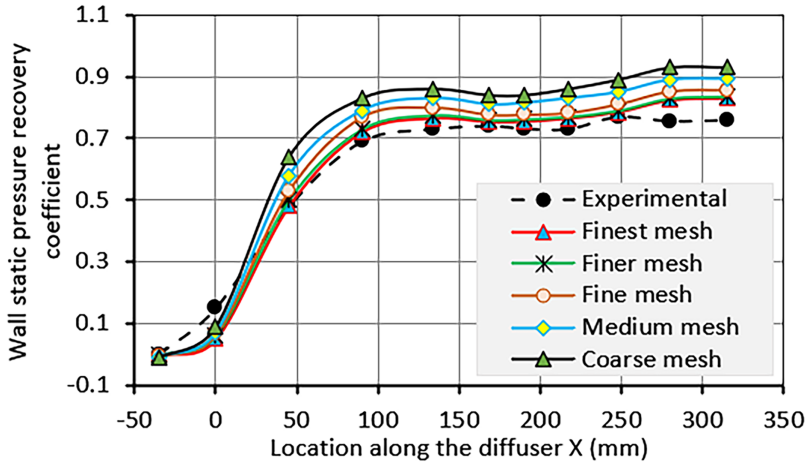


Figure 5: Wall static pressure coefficient, C_{WPR} on the top surface of AD/VG-2 with different mesh configurations compared to experimental data.

2.4.2 Boundary Conditions

The CFD simulations of diffuser models use *Uav.in*, p and TI values measured experimentally as input boundary conditions. For all simulation cases, zero-gauge pressure was specified as an exit boundary condition. A no-slip boundary condition was specified at the walls of the diffuser. Near the wall, modeling is performed with an enhanced wall treatment method to address the boundary layer formed during grid generation. Finally, all simulation cases were performed with standard air conditioning, as presented in Table 7.

Table 7: Description of boundary conditions.

Boundary	Condition
Inlet Boundary Conditions	
Type of boundary	Velocity–inlet
Inlet velocity (m/s)	9.8
Corresponding Re	40,000
Turbulence intensity %	4.5%
Outlet Boundary Conditions	
Type of boundary	Pressure–outlet
Pressure (Pa)	0-gauge
Wall Boundary Conditions	
Type of boundary	Roughness
Shear condition	no–slip
Working Fluid Properties	
Working fluid	Air
Density (kg/m^3)	1.165
Viscosity (kg/m·s)	1.858×10^{-5}

3 Results and Discussion

Two methods of flow visualization, namely, experimental and computational, were used to characterize the flow structure within S-shaped diffusers. Five different diffusers were investigated with 40,000 Re at the inlet. This section explains and discusses the flow behavior inside BD, AD and AD-VGs with the presence of different configurations of VGs, through the velocity vectors of the longitudinal plane at the middle of the diffuser.

3.1 Validation of the Numerical Results against the Experimental Results

Computational procedures require validation by quantitative performance parameter comparison against experimental measurement results. The flow field is computationally simulated using the standard k-ε turbulence model. The selected performance parameter is the wall static pressure recovery coefficient (C_{WPR}) at the top and bottom surfaces. Fig. 6a shows the comparison between the experimental and numerical results of C_{WPR} on the top surface. The results show that the maximum experimental C_{WPR} of 0.62 is higher than the maximum numerical C_{WPR} of 0.57. Fig. 6b shows the comparison between the experimental results and the numerical results of C_{WPR} on the bottom surface. The trend between experimental and numerical results is rather similar, with some differences. The experimental maximum C_{WPR} is 0.556, while it is 0.514 by computational prediction. In conclusion, the percentage differences in the maximum C_{WPR} values are 8.4% at the top surface and 7.8% at the bottom surface. Given the flow type, with separation and high reversal flow, the computational procedure is considered valid as the maximum percentage difference is less than 10%.

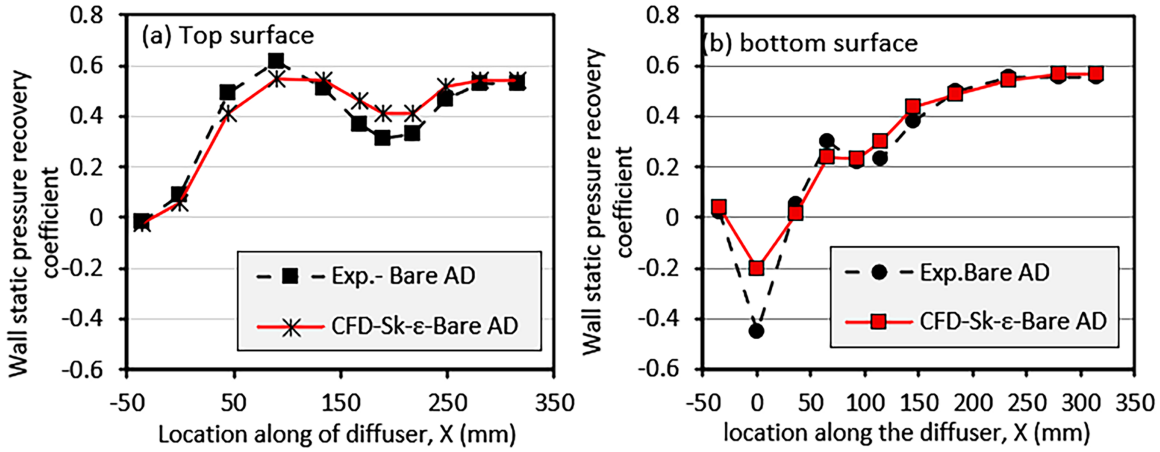


Figure 6: Comparison of the experimental results against the simulation results with different turbulence models of C_{WPR} of bare AD on: (**a**) top surface, (**b**) bottom surface.

3.2 Visualization Analysis of Bare S-Shaped Diffuser

Fig. 7 shows the flow visualization of BD. The lines of wall-mounted tufts show the flow Behavior on the bottom surface. It is visible that the flow separation and reverse flow start at around $L_{s.p.}$ = 0.4 from the unsteady motion of tufts and the tendency to lift from the surface, as shown by the bounded red circle. The flow separation zone and reversed flow persist until the region between plane 8 and plane 9, close to the outlet plane. This refers to a large amount of reversed and separated flow.

The computational simulation results of the flow velocity along the axial axis of the BD are shown in Fig. 8. After the inlet plane, the longitudinal velocity profile tends to distort towards the bottom surface due to the high curvature of the bottom surface of the diffuser. The flow near the top surface is decelerated until the first bend at approximately X/L_s = 0.3 for the BD. After the first bend, the flow accelerates at the top surface and decelerates at the bottom surface, reaching the outlet (plane 9). This flow behavior is due to the secondary flow resulting from the increased flow separation zone at the bottom surface.

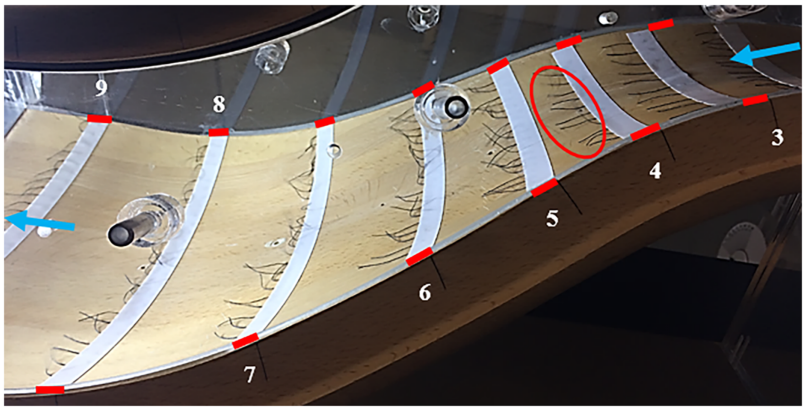


Figure 7: Flow visualization on the bottom surface of bare diffuser (BD) using wall-mounted tufts.

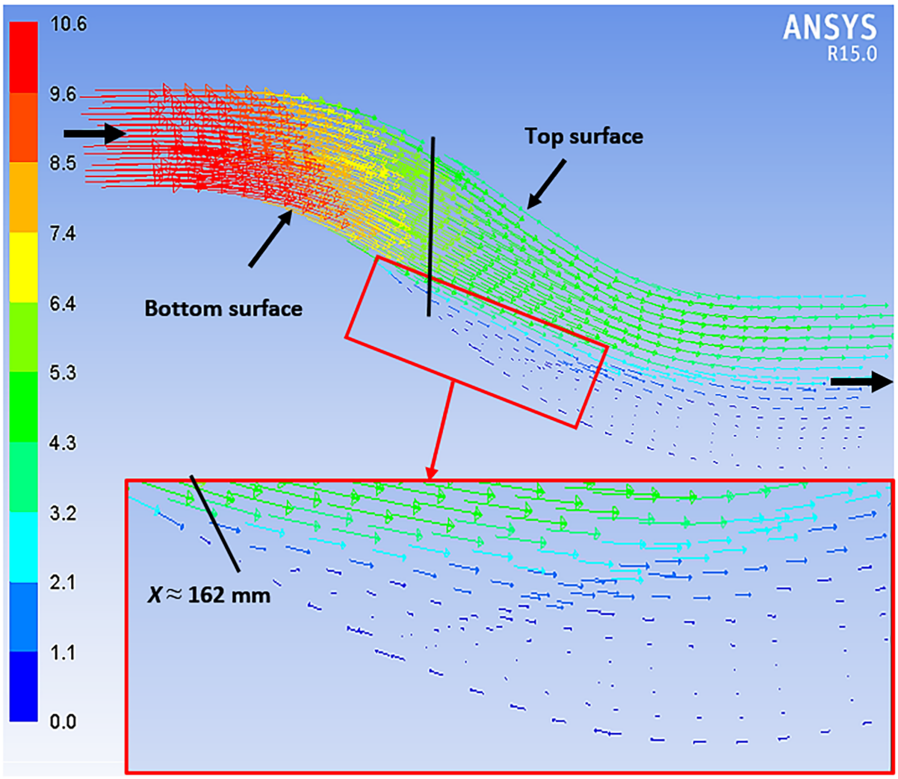


Figure 8: Computational simulation results of the velocity vector of the flow field in the bare diffuser (BD) colored by velocity magnitude (m/s), with enlarged flow separation zone.

The velocity vectors indicate that separation begins approximately at $L_{s.p.}$ = 0.406 on the bottom surface. The reversed and separated flow could be seen from the onset of flow separation until the outlet plane of the diffuser, after plane 8 and before plane 9. The separation point occurred at $L_{s.p.}$ = 0.4 and 0.406, as indicated by the experimental and computational visualizations, respectively.

3.3 Visualization Analysis of Aggressive S-Shaped Diffuser

Fig. 9 shows the flow visualization of the bare AD captured in the experimental visualization. The flow separation and reverse flow are visible from the line of wall tufts after plane 3, at around $L_{s.p.} \approx 0.3$. The unsteady motion of tufts and tendency to lift from the surface show a strong reversed and large separation bubble compared to the visualization of the BD. The separated flow regime occurs within the entire zone from plane 4 to plane 9.

The predicted development of flow velocity along AD, as visualized in the computational visualization, is shown in Fig. 10. After the inlet plane, the longitudinal velocity profile tends to distort towards the bottom surface due to the shape of the bottom surface of the diffuser, in addition to high curvature at the first bend.

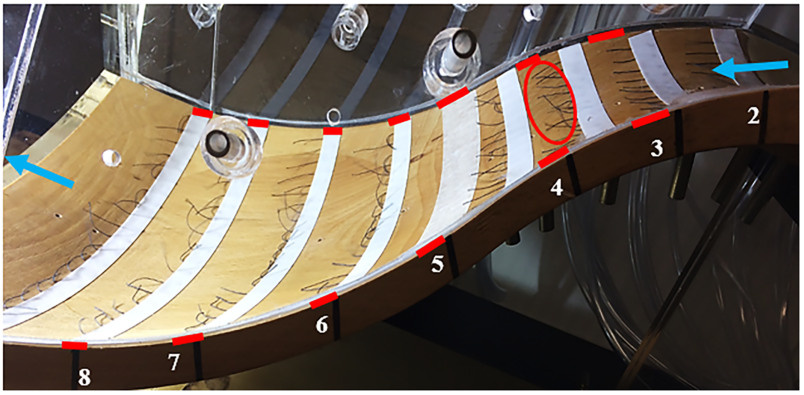


Figure 9: Flow visualization on the bottom surface of the aggressive S-shaped diffuser using wall-mounted tufts.

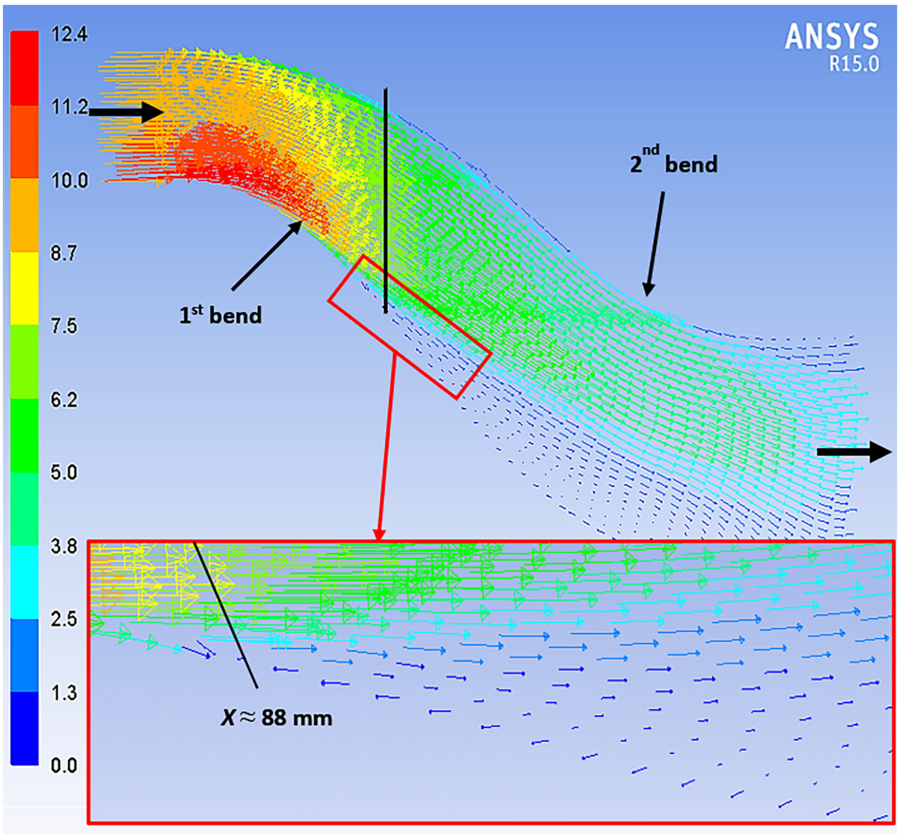


Figure 10: Computational simulation results of the velocity vector of the flow field in the aggressive S-diffuser (AD), colored by velocity magnitude (m/s), with an enlarged flow separation zone.

On the bottom surface of the AD, the flow at the first bend undergoes greater acceleration and, consequently, greater diffusion due to the smaller radius of curvature. This part of the flow was found to handle a significant part of the overall duct total pressure loss caused by a thick low-pressure region (flow separation zone) at the bottom surface occupying a large zone of the AD area compared to the BD. This thicker boundary layer reduces the effective local diffuser area and therefore less static pressure is recovered. Flow separation started at $L_{s.p.}$ = 0.314 on the bottom surface of the AD. For both setups, BD and AD, the

already described redistributed high-loss fluid in the mid-pitch casing region, i.e., the high curvature zone, was observed, but more pronounced for the shorter diffuser. This process was also observed by other studies like Norris and Dominy [26].

3.4 Visualization Analysis of an Aggressive Diffuser Fitted with Vertex Generators Type-1

Fig. 11 shows the flow visualization on the bottom surface of AD/VG-1, where a significant improvement in the flow field is indicated by high uniformity and less reverse flow by employing the VGs type-1 at plane 5. The small area of reverse flow indicates that small reverse flow takes place, and this process is observed at $L_{s.p.} \approx 0.67$. The higher reduction in flow separation results in small pressure loss and increases the static pressure and the flow uniformity at the outlet plane. Thereby, the performance improvement of AD/VG-1 was increased.

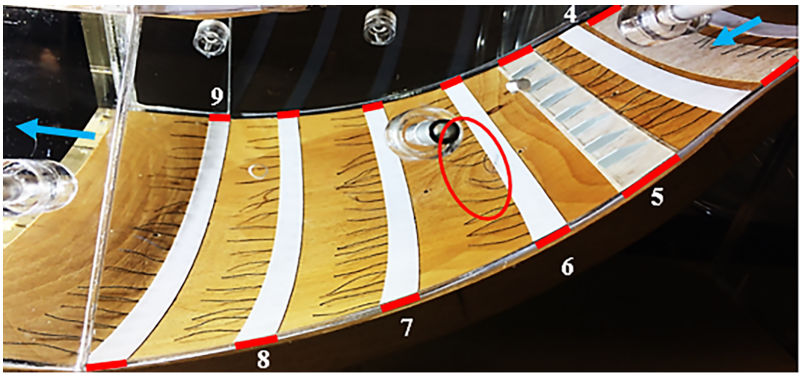


Figure 11: Flow visualization on the bottom surface of the aggressive S-shaped diffuser fitted with VGs type-1 using wall-mounted tufts.

Fig. 12 shows the longitudinal velocity vectors of AD/VG-1 with VGs type-1 at plane 5. The effect of VGs is clear on flow structure improvement through delaying the start of flow separation, eliminating or removing flow separation, in addition to improving the flow uniformity at the outlet plane. Adding VGs type-1 to the AD has delayed the start of flow separation until $L_{s.p.} \approx 0.63$. Moreover, the size of the separation zone and reverse flow were reduced so much as shown in the expanded views of Fig. 12. Also, the flow became more uniform at the outlet plane and had less deviation between the maximum and minimum values compared with bare BD and AD.

3.5 Visualization Analysis of Aggressive Diffuser Fitted with Energy Promotors Type-2

Fig. 13 shows the flow visualization on the bottom surface of AD/VG-2, indicating a significant improvement in the flow with high uniformity and much less reverse flow. The small area of the tuft lifting from the surface indicates that no flow separation occurs, and this process is observed at plane 6. The higher reduction in flow separation results in a small loss of pressure and increases the static pressure and the flow uniformity at the outlet plane. Thereby, the performance improvement of AD/VGs was increased, and the best improvement was achieved by using VGs type-2 at plane 5.

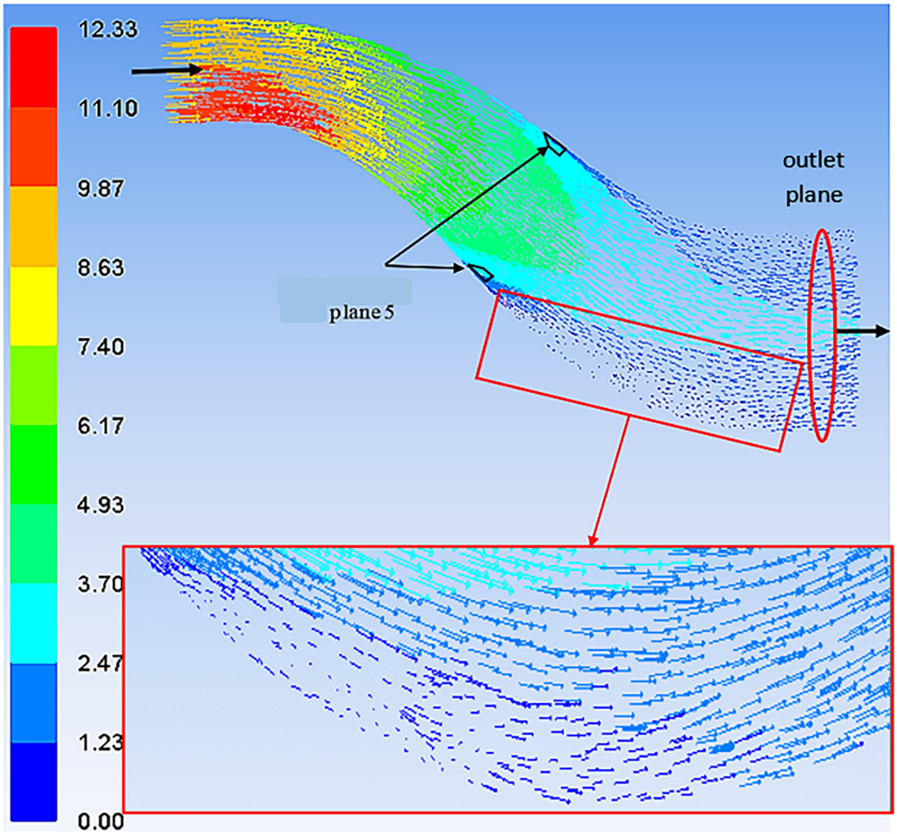


Figure 12: Velocity vectors in the aggressive S-shaped diffuser fitted with VGs type-1, colored by velocity magnitude (m/s), with enlarged flow separation zone.

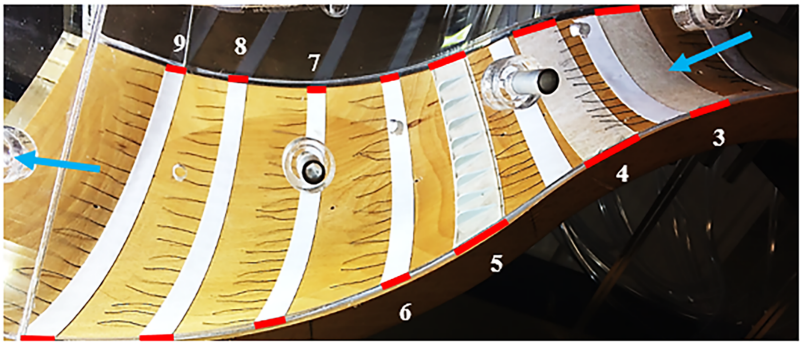


Figure 13: Flow visualization on the bottom surface of the aggressive S-shaped diffuser fitted with VGs type-2 using wall-mounted tufts.

Obviously, from Fig. 14, by employing VGs type-2 at plane 5 of AD/VG, the flow separation has been removed completely and increases the uniformity of flow at the outlet, plane 9. Also, the average outlet velocity has decreased to about 1.8 m/s, with a large area in this range. This process enhances the performance of AD/VG through increasing the static pressure recovery coefficient, C_{PR} and decreasing the total pressure loss coefficient, C_{TL} and distortion coefficient, $DC(45°)$.

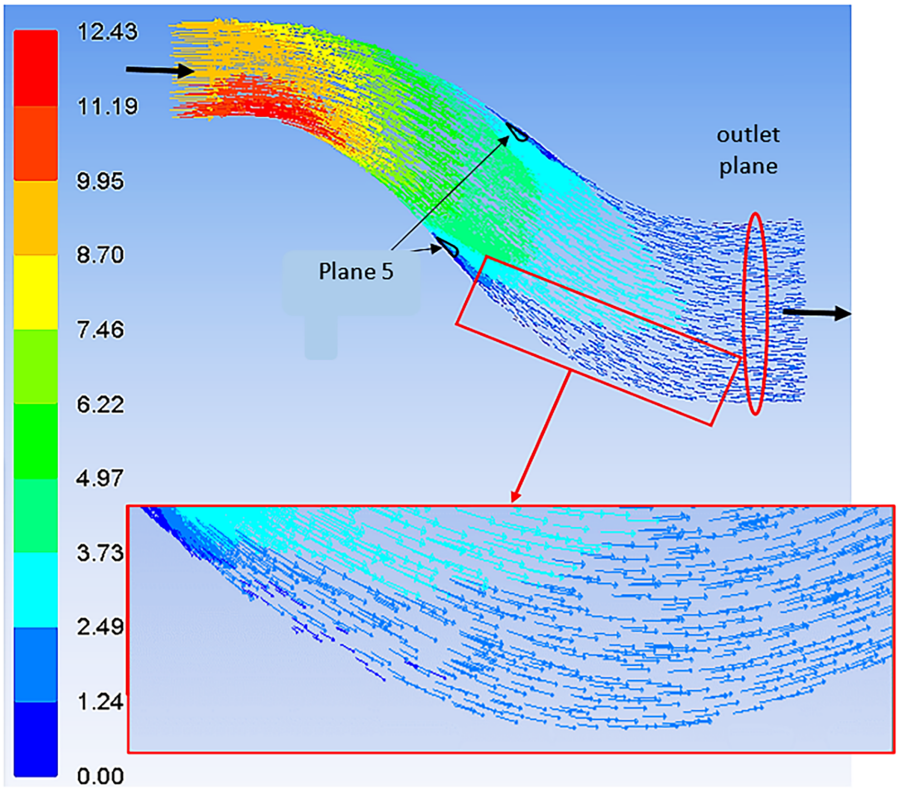


Figure 14: Longitudinal velocity vectors with the flow separation zone of AD/VG-2.

3.6 Visualization Analysis of Aggressive Diffuser Fitted with Vortex Generators Type-3

The visualization in Fig. 15 shows the tuft uniformity destruction on the bottom surface of AD/VG-3. The installation of VGs type-3 in the lower surface of the S-shaped diffuser resulted in more flow uniformity. The reverse flow is highly reduced with the use of VGs type-3. A significant improvement in the streamwise airflow with high uniformity and a highly reduced value with the use of VGs type-3. A small reverse flow takes place on plane 7, at $L_{s.p.} \approx 0.78$.

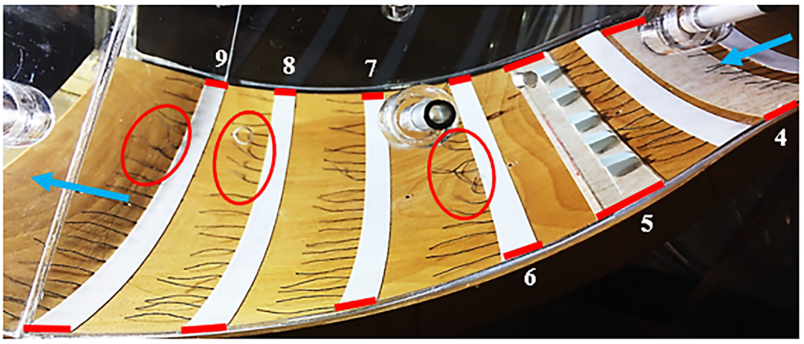


Figure 15: Flow visualization on the bottom surface of the aggressive S-shaped diffuser fitted with VGs type-3 using wall-mounted tufts.

Fig. 16 shows the longitudinal vectors of AD/VG with VGs type-3 employed at plane 5. These VGs could delay the start of flow separation and reduce the size of the separation zone compared to the bare AD. But the

flow uniformity is less compared to the two other types of VGs due to the high flow velocity at the core of the outlet plane cross-section. This results in less improvement of C_{PR} and less reduction in $DC(45°)$ compared to the other two types of VGs investigated.

Use of VGs type-3 resulted in the flow structure shown in Fig. 16. Improvement in the flow behavior was achieved by suppressing the flow separation except for small zones observed at planes 6, 8 and 9. It is noticed that the tufts are lifting up at those planes. The separation point is located at $L_{s.p.} \approx 0.8$. This process results in a decrease in total pressure loss and the distortion coefficient, thereby increasing the static pressure and improving flow uniformity at the exit of the S-shaped diffuser.

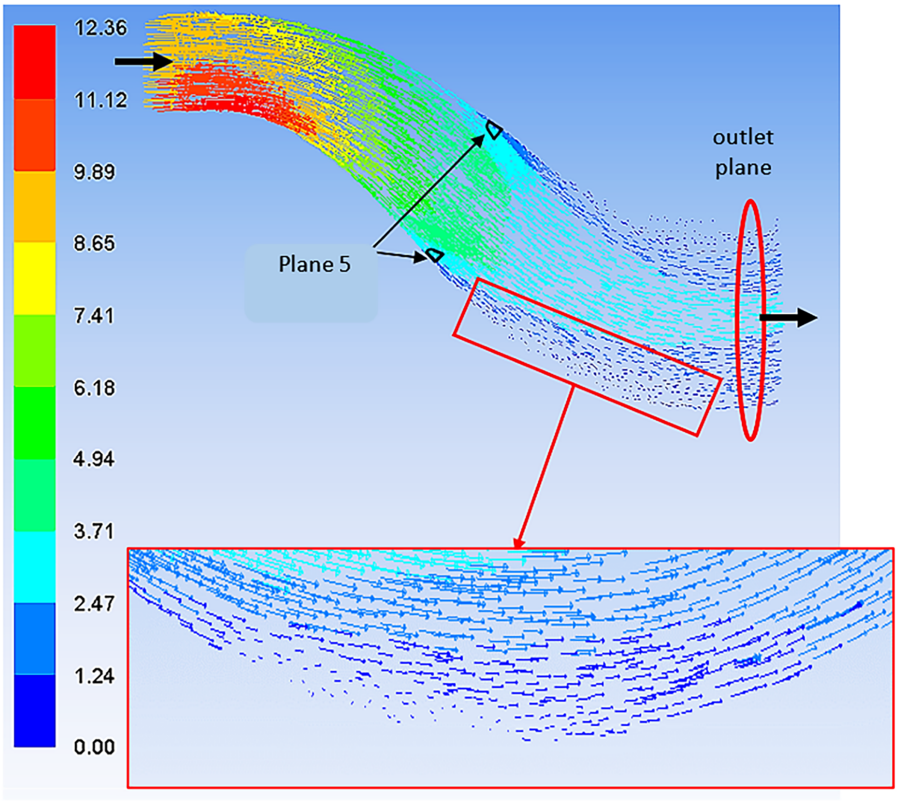


Figure 16: Longitudinal velocity vectors with the flow separation zone of AD/VG-3.

3.7 Summary of the Findings

The flow visualization test by wall-mounted tufts has been conducted on the bottom surface of BD, AD and AD/VG with three types of VGs with inlet Re = 40,000. The purpose of these investigations is to identify the best VGs type that can achieve a high reduction in pressure loss, eliminate or reduce flow separation, and thereby increase the static pressure and flow uniformity at the outlet plane of the S-shaped diffuser. A Summary of the main findings is presented in Table 8. The investigation results show that implementing the three types of VGs at plane 5 improved the performance of AD/VG compared to bare AD. However, VGs of type 2 have resulted in a significant improvement in flow at the outlet plane by suppressing flow separation to the maximum extent and increasing flow uniformity. The separation point is located approximately, at $L_{s.p.}$ = 0.4, 0.3, 0.678, and 0.78, and numerically at 0.406, 0.314, 0.638, and 0.8 for BD, AD, and AD/VG-1, and AD/VG-3, respectively, while no separation occurred in the case of AD/VG-2.

Table 8: The conclusions of the five visualized S-shaped diffusers.

Case	Location of Separation Point along the Axial Axis $L_{s.p.}$		Main Conclusions on the Separation Zone	Observations on the Diffuser Performance
	Exp.	Comp.		
Bare diffuser (BD)	0.4	0.406	Reversal flow extends till the midplane between planes 8 and 9.	Considerable destruction of the flow uniformity at the exit of the diffuser.
Aggressive diffuser (AD)	0.3	0.314	The separated flow occurs within the entire zone from plane 4 to plane 9.	The thicker boundary layer reduces the effective diffuser area and therefore less static pressure is recovered, and larger uniformity destruction compared to BD.
Aggressive diffuser fitted with VG type-1 (AD/VG-1)	0.678	0.638	A small area of reverse flow indicates the effectiveness of the VGs to control the flow.	Less flow uniformity destruction at the exit compared to the BD and AD cases.
Aggressive diffuser fitted with VG type-2 (AD/VG-2)	No separation	No separation	VGs type-2 eliminated the reversal flow.	The best performance was achieved, and the flow uniformity is higher compared to all other cases.
Aggressive diffuser fitted with VG type-3 (AD/VG-3)	0.78	0.8	A small separation bubble and the reversal flow were observed at planes 6 to 9.	Flow uniformity is less compared to the two other types of VGs due to the high flow velocity at the core of the outlet plane cross-section.

The higher reduction in flow separation results in a small loss of pressure and increases the static pressure and the flow uniformity at the outlet plane. Thereby, the performance improvement of AD/VGs was increased, and the best improvement was achieved by using the VGs type-2.

Table 9 displays the measured and predicted flow distortion using Eq. (2) for all cases. The length reduction drastically reduced flow uniformity at the diffuser exit, where the results show increased distortion of the AD compared to the BD by 11.9% experimentally, and 9.6% numerically. Installation of the VGs showed significant improvement, as they reduced the distortion caused by the aggressive diffuser. From the experimental visualization, the distortion in the aggressive S-shaped diffuser is reduced by 71.8%, 87.8%, and

29.7% by VG-1, VG-2, and VG-3, respectively. The predicted reductions from computational visualization are 44.6%, 88%, and 36.2% by VG-1, VG-2, and VG-3, respectively. The highest reduction in flow distortion is achieved by VG type-2 due to its streamlined upper edge, which does not result in local rotation or the creation of small vortices, in contrast to VG-1, which is not streamlined and results in highly disturbed flow at the upper edge of the VG.

Table 9: The experimentally measured and numerically predicted distortion coefficient.

***DC*(45°)**	**Type of S-Shaped Diffuser**				
	BD	**AD**	**AD/VG-1**	**AD/VG-2**	**AD/VG-3**
Experimental	0.177	0.201	0.117	0.107	0.155
Numerical	0.17	0.188	0.13	0.10	0.138

4 Conclusions

The flow development and structures inside the bare S-shaped diffuser (BD), the Aggressive S-shaped diffuser (AD), and the S-shaped aggressive diffuser fitted with three types of passive flow-control vortex generators (AD/VG) have been qualitatively visualized experimentally using wall tufts and computationally using CFD. The investigations have been carried out at an inlet Re of 40,000. Results revealed reversal flow in the cases of BD, AD, AD/VG-1, and AD/VG-3. The AD showed earlier separation and a larger separation bubble than the BD, with the separation point occurring around 35% earlier on the lower surface of the diffuser. However, the VGs illustration has significantly improved the flow structure and delayed separation in the aggressive diffuser. Installation of VGs type-2, a co-rotating streamline sheet, eliminated flow separation and reduced flow destruction by 87.8% experimentally and 88% numerically. The work demonstrates that computational flow visualization complements and extensively improves the analysis of experimental visualization using wall-mounted tufts. Adopting both techniques to complement each other is recommended for gaining insight, understanding and characterizing complex flows with large separation bubbles.

Acknowledgement: The authors acknowledge Universiti Teknologi PETRONAS, Malaysia, for the logistic and technical support by allowing the experimental investigations to be performed in the Advanced Fluid Dynamic Lab, Mechanical Engineering Department. In particular, Dr. Raed would like to express his thankfulness to UTP for the financial support under the Graduate Assistance (GA) scheme during his PhD study.

Funding Statement: The authors received no specific funding for this study.

Author Contributions: The authors confirm contribution to the paper as follows: Conceptualization, Hussain H. Al-Kayiem, Ali M. Mohsen, Raed A. Jessam; methodology, Hussain H. Al-Kayiem, Raed A. Jessam; software, Hussain H. Al-Kayiem, Ali M. Mohsen, Ajyal A. Hassan Jallout, Ali M. Tukkee, Raed A. Jessam; validation, Hussain H. Al-Kayiem, Raed A. Jessam; formal analysis, Hussain H. Al-Kayiem, Ali M. Mohsen, Ajyal A. Hassan Jallout, Ali M. Tukkee, Raed A. Jessam; investigation, Raed A. Jessam; data curation, Hussain H. Al-Kayiem, Ali M. Mohsen, Ajyal A. Hassan Jallout, Ali M. Tukkee, Raed A. Jessam; writing—original draft preparation, Raed A. Jessam; writing—review and editing, Hussain H. Al-Kayiem, Ali M. Mohsen, Ajyal A. Hassan Jallout, Ali M. Tukkee; visualization, Hussain H. Al-Kayiem, Raed A. Jessam; supervision, Hussain H. Al-Kayiem. All authors reviewed and approved the final version of the manuscript.

Availability of Data and Materials: The data that support the findings of this study are available from the Corresponding Author, [Hussain H. Al-Kayiem], upon reasonable request.

Ethics Approval: Not applicable.

Conflicts of Interest: The authors declare no conflicts of interest.

References

1. Saha K, Singh SN, Seshadri V, Mukhopadhyay S. Computational analysis on flow through transition S-diffusers: effect of inlet shape. J Aircr. 2007;44(1):187–93. doi:10.2514/1.22828.
2. Wellborn SR, Okiishi TH, Reichert BA. A study of the compressible flow through a diffusing S-duct. Washington, DC, USA: NASA; 1993. Report No.: NASA-TM-106411.
3. Paul AR, Ranjan P, Patel VK, Jain A. Comparative studies on flow control in rectangular S-duct diffuser using submerged-Vortex generators. Aerosp Sci Technol. 2013;28(1):332–43. doi:10.1016/j.ast.2012.11.014.
4. Al-Kayiem HH, Ali SM, Al-Azawiey SS, Jessam RA. A comparative review of the experimental mitigation methods of the S-shaped diffusers in the aeroengine intakes. Energy Eng. 2026;123(2):1–10. doi:10.32604/ee.2025.073303.
5. Teng J, Feng J, Wu D, He P, Zhu M. Flow development through an S-shaped diffusing duct. Int J Turbo Jet Engines. 2022;39(4):513–23. doi:10.1515/tjj-2019-0045.
6. Jessam R, Al-Kayiem H, Al-Azawey S. Experimental assessment of S-diffuser performance in the aeroengine intake by installation of energy promotors. J Eng Sci Technol. 2026;21(1):249–67.
7. Kooshartoyo M, Yohana E, Muchammad M, Pane IZ. Visualization analysis of flow with smoke on airfoils and flaps. J Adv Res Exp Fluid Mech Heat Transf. 2025;21(1):70–6. doi:10.37934/arefmht.21.1.7076.
8. He B, Li G, Zhou F, Liu D, Xiang X. Application of colour fluorescent oil flow visualization for a high speed cavity. J Phys Conf Ser. 2021;1786(1):012049. doi:10.1088/1742-6596/1786/1/012049.
9. De Voogt F, Ganapathisubramani B. Determination of unsteady wing loading using tuft visualization. Exp Fluids. 2024;65(10):148. doi:10.1007/s00348-024-03882-1.
10. Padwad PV, Govardhan M. Flow and performance characteristics of S-shaped diffusers. Int J Fluid Mech Res. 2010;37(6):553–66. doi:10.1615/interjfluidmechres.v37.i6.40.
11. Menzies R. Computational investigation of flows in diffusing S-shaped intakes. Acta Polytech. 2001;41(4–5):61–7. doi:10.14311/262.
12. Kassim MS, Sadeq MS, Aljibori HS, Mahmood RA. Enhancing forced convective heat transfer in a sinusoidal duct by insertion of porous material. J Eng Sci Technol. 2023:194–209.
13. Krishna VM, Sandeep Kumar M, Mahesh O, Senthil Kumar P. Numerical investigation of heat transfer and pressure drop for cooling of microchannel heat sink using MWCNT-CuO-Water hybrid nanofluid with different mixture ratio. Mater Today Proc. 2021;42:969–74. doi:10.1016/j.matpr.2020.11.935.
14. Soehartanto T, Putu Eka Widya Pratama I, Putra AD. The design of fuel dryer in palm oil processing industries by utilizing the heat product of boiler based on computational fluid dynamic. IOP Conf Ser Earth Environ Sci. 2022;1034(1):012008. doi:10.1088/1755-1315/1034/1/012008.
15. Chen L, Suzuki T, Nonomura T, Asai K. Characterization of luminescent mini-tufts in quantitative flow visualization experiments: surface flow analysis and modelization. Exp Therm Fluid Sci. 2019;103(8):406–17. doi:10.1016/j.expthermflusci.2019.02.002.
16. Neves AF, Lawson NJ, Bennett CJ, Khanal B, Hoff RI. Unsteady aerodynamics analysis and modelling of a Slingsby Firefly aircraft: Detached-Eddy Simulation model and flight test validation. Aerosp Sci Technol. 2020;106(5):106179. doi:10.1016/j.ast.2020.106179.
17. Cai C, Zuo Z, Liu S, Maeda T. Effect of a single leading-edge protuberance on NACA 634-021 airfoil performance. J Fluids Eng. 2018;140(2):021108. doi:10.1115/1.4037980.
18. Chen L, Suzuki T, Nonomura T, Asai K. Flow visualization and transient behavior analysis of luminescent mini-tufts after a backward-facing step. Flow Meas Instrum. 2020;71(1):101657. doi:10.1016/j.flowmeasinst.2019.101657.
19. Vey S, Lang HM, Nayeri CN, Paschereit CO, Pechlivanoglou G. Extracting quantitative data from tuft flow visualizations on utility scale wind turbines. J Phys Conf Ser. 2014;524(1):012011. doi:10.1088/1742-6596/524/1/012011.
20. Swytink-Binnema N, Johnson DA. Digital tuft analysis of stall on operational wind turbines. Wind Energy. 2016;19(4):703–15. doi:10.1002/we.1860.

21. Steinfurth B, Cura C, Gehring J, Weiss J. Tuft deflection velocimetry: a simple method to extract quantitative flow field information. Exp Fluids. 2020;61(6):146. doi:10.1007/s00348-020-02979-7.
22. Jia W, Xu H. Strategies for energy-efficient flow control leveraging deep reinforcement learning. Eng Appl Artif Intell. 2025;156(6):111125. doi:10.1016/j.engappai.2025.111125.
23. Gad-el-Hak M, Bushnell DM. Separation control: review. J Fluids Eng. 1991;113(1):5–30. doi:10.1115/1.2926497.
24. Al-Kayiem HH, Jessam RA, Hamdi SS, Tukkee AM. Numerical evaluation of the performance enhancement of S-shaped diffuser at the intake of gas turbine by energy promoters. Energy Eng. 2025;122(4):1311–35. doi:10.32604/ee.2025.061709.
25. Kumaraswamy R, Natarajan K, Anand RB. CFD analysis of flow and performance characteristics of a 90°curved rectangular diffuser: effects of aspect ratio and Reynolds number. Int J Turbo Jet Engines. 2021;38(4):451–63. doi:10.1515/tjj-2019-0011.
26. Norris G, Dominy RG. Diffusion rate influences on inter-turbine diffusers. Proc Inst Mech Eng Part A J Power Energy. 1997;211(3):235–42. doi:10.1243/0957650971537141.